Journal of Environmental Chemical Engineering 12 (2024) 111805

Contents lists available at ScienceDirect

Journal of Environmental Chemical Engineering

journal homepage: www.elsevier.com/locate/jece

The optimized microbial-induced calcium carbonate precipitation process to fabricate underwater superoleophobic mesh for efficient oil-water separation

Sikai Tang [a], Yuze Wang [a,*]

[a] Department of Ocean Science and Engineering, Southern University of Science and Technology, Shenzhen 518005, China

ARTICLE INFO

Editor: Dong-Yeun Koh

Keywords:
Microbial-induced calcium carbonate precipitation (MICP)
Environmental factors
Wettability
Oil-water separation
Stainless steel mesh

ABSTRACT

Microbial-induced calcium carbonate precipitation (MICP) is an environmentally-friendly and easy operation technique for separating oil-water mixtures. However, the effect of environmental factors on the wettability and oil-water separation performance of MICP remains unclear. In this study, three primary factors including mineralization solution (MS) concentration, bacterial suspension (BS) concentration, and temperature were carefully investigated. Under these varying conditions, stainless steel meshes (SSM) were chosen as the substrates for the growth of $CaCO_3$ precipitations. Experimental results demonstrate a strong dependence of the morphology and wettability of $CaCO_3$ precipitations on these factors. Higher MS concentration and temperature contribute to enhanced hydrophilicity of $CaCO_3$ coatings due to the increased surface roughness. The water flux of MICP-coated SSMs decreases with the increase of BS concentration, MS concentration, and temperature. The MICP-coated SSM obtained with MS concentration of 0.15 M, BS concentration of 0.1×10^8 cells/mL, and mineralization reaction at 25 ℃ for 24 hours demonstrated the optimal comprehensive performance, exhibiting underwater superoleophobicity with an underwater oil contact angle (UWOCA) exceeding 151°, an ultra-high oil intrusion pressure (> 3.0 kPa), ultrahigh flux (28,644 L m^{-2} h^{-1}), and a preferable oil rejection rate (> 99.9%). Additionally, the as-prepared mesh exhibited superior anti-oil-fouling property and reusability, while concurrently demonstrating excellent chemical and thermal stability. This work contributes to advancing our knowledge of the influence of various environmental factors on the wetting characteristics of MICP and provides a feasible solution for the highly efficient and low-cost preparation of oil-water separation membranes based on the MICP process.

1. Introduction

Frequent marine oil spill accidents and the discharge of industrial oily wastewater pose tremendous hazards to marine ecosystems, as well as to human production and livelihoods [1–3]. Although many methods, including adsorption [4], oil skimming [5], centrifugation [6], and flocculation [7], etc., have been developed for the treatment of oily wastewater in response to the environmental challenges posed by oil pollution, these methods still face limitations in terms of low separation efficiency, high cost, large footprint, and the risk of secondary pollution. Therefore, more efficient, environmentally-friendly, and convenient methods are urgently desired. In recent years, there has been extensive development of superwetting membrane materials for highly efficient oil-water separation, utilizing substrates such as metal meshes [8-10], cellulose membranes [11], textiles [12-14], papers [15], woods [16,17] and so on [2,18]. Among them, metal meshes have been extensively studied as substrates for superwetting membranes due to their high separation flux, easy availability, excellent mechanical properties, and easy surface modification [19,20]. Various superhydrophobic and superoleophilic meshes, so-called "oil-removing" meshes, have attracted considerable attention for oil-water separation due to their remarkable corrosion resistance and self-cleaning properties [21,22]. These meshes have the ability to allow oil to penetrate while blocking water, thus achieving the oil-water separation. However, these oil-removing meshes could be easily contaminated and clogged by adhered oil due to their high oil affinity, leading to a decreased separation efficiency, flux, and reusability [23]. Additionally, gravity-driven oil-removing meshes are very difficult to efficiently separate oil-water mixtures, because most

* Corresponding author
E-mail address: wangyz@sustech.edu.cn (Y. Wang).

https://doi.org/10.1016/j.jece.2023.111805
Received 6 October 2023; Received in revised form 13 December 2023; Accepted 22 December 2023
Available online 26 December 2023

oils have a lower density than water, resulting in the water layer preventing oil penetration.

Inspired by the underwater oil-repellence of fish scales, superhydrophilic and underwater superoleophobic meshes, namely "water-removing" meshes, have been developed to address the above limitations [24,25]. Due to the strong affinity towards water, a stable water film is formed between the oil and the mesh, effectively preventing direct contact between the oil and the mesh surface [26]. This type of mesh can be achieved through hydrophilic composition modification and the construction of micro/nanostructures [27,28]. For instance, Chen et al. [29] fabricated an underwater superoleophobic mesh by coating TiO_2 nanoparticles onto the stainless steel mesh via a self-assembly method. The as-prepared TiO_2 coated mesh showed a very high filtration flux of 54000 L m^{-2} h^{-1} and a separation efficiency exceeding 99%. Meanwhile, various kinds of materials such as NaA zeolites [30], MgAlZn layered double hydroxides [31], ZnO nanowires [32], metal-organic frameworks (MOFs) [33], and polyvinyl alcohol (PVA)-sodium silicate composites [34] have been successfully coated onto the metal meshes endowing them a superhydrophilic and underwater superoleophobic properties. However, most of these materials still face many limitations such as poor structural stability, complex fabrication process, special equipment, use of hazardous chemicals, and weak environmental adaptability. It is still a big challenge to fabricate novel oil-water separation metal meshes via facile, environmental-friendly, and low-cost approaches.

Shell nacre, mainly composed of biominerals with hierarchical micro/nanostructures, exhibit excellent superhydrophilicity and underwater superoleophobicity [35,36]. As is known, the biominerals in shell nacre are mainly composed of calcium carbonate ($CaCO_3$), which is an intrinsic hydrophilic compound owing to the abundant hydrophilic hydroxyl groups on its surface [37]. Therefore, a biomimetic mineralization approach, inspired by the surface of nacre, has been extensively utilized for the fabrication of superhydrophilic and underwater superoleophobic meshes. For example, Dai et al. [38] prepared a nacre-like graphene oxide-$CaCO_3$ hybrid stainless steel mesh via a layer-by-layer self-assembly method. The as-prepared mesh demonstrated superhydrophilicity and underwater superoleophobicity, and it showed outstanding oil-water separation performance. Yu et al. [39] deposited $CaCO_3$ particles onto the methacrylated chitosan hydrogel-coated mesh via biomineralization and dip coating methods using poly(acrylic acid) as an additive. The synthesized mesh exhibited excellent separation efficiency ($>$ 99.99%) and mechanical stability. It is noteworthy that the conventional biomimetic mineralization processes of $CaCO_3$ have non-negligible drawbacks such as complicated preparation process, macroscopic structural discontinuity, non-uniformity and additional polymer additives. Importantly, the wettability of the micro/-nano-$CaCO_3$ coating is largely affected by its macroscopic structural continuity and uniformity, which in turn depends on whether there are enough heterogeneous nucleation sites and strong adhesion force of reactants in mineralization process [40]. Actually, the microbial-induced calcium carbonate precipitation (MICP) technique, could easily realize the formation of a dense $CaCO_3$ layer with micro/-nanostructures. This technique has been successfully applied for the remediation of cultural heritages [41], sand solidification [42,43], concrete reinforcement [44], anti-corrosion [45], and heavy metal contaminants treatment [46]. Very recently, studies have demonstrated that dense $CaCO_3$ particles can be spontaneously formed on the surface of SSMs with the help of bacteria, and the resulting meshes have been successfully applied to separate oil-water mixtures [47,48]. However, previous studies have not thoroughly investigated the influence of environmental factors, which directly affect the surface morphology, structure, and wettability of minerals. Moreover, the time and material costs of the previous works were relatively high, which was not conductive to future large-scale production.

In this study, superhydrophilic MICP-coated SSMs for oil-water separation were prepared under various environmental conditions with the assistance of a high urease-producing bacterial strain of *S. pasteurii*. Material characterization techniques including SEM, EDS, XRD, white light interferometer, and contact angle measuring instrument were applied to investigate the morphology, surface roughness, and wettability of the MICP coating under different environmental factors, respectively. The MICP-coated SSM obtained under the optimal conditions showed superhydrophilicity/underwater superoleophobicity, ultra-high oil intrusion pressure, and excellent oil-water separation performance, while concurrently demonstrating superior anti-oil-fouling property, ideal mechanical/chemical/thermal stability, and outstanding recyclability.

2. Experimental materials and methods

2.1. Materials

Sporosarcina pasteurii (*S. pasteurii*, CGMCC 1.3687), a typical ureolytic bacterial strain, was obtained from China General Microbiological Culture Collection Center. The 304 stainless steel mesh (500 mesh, pore size of 25 μm) was purchased from Changzhou Tezhende Metal Products Co., Ltd (Changzhou, China). Calcium chloride dihydrate ($CaCl_2{\cdot}2\ H_2O$), anhydrous ethanol, oil red O, methylene blue, hexane, petroleum ether, and dichloromethane (DCM) were purchased from Shanghai Macklin Biochemical Technology Co., Ltd (Shanghai, China). Urea ($CO(NH_2)_2$, 99.5%), Tris (hydroxymethyl) aminomethane (Tris base, 99.9%), and ammonium sulfate ($(NH_4)_2SO_4$, 99%) were purchased from Aladdin Biochemical Technology Co., Ltd (Shanghai, China). Yeast extract was produced by Oxoid Ltd (Basingstoke, UK). Nutrient broth was purchased from Guangdong Huankai Microbial Technology Co., Ltd (Guangzhou, China). Diesel was bought from the local Sinopec gas station. Machine oil and soybean oil were obtained from a local supermarket. Deionized water (DI water) was obtained from the ultrapure water system (Milli Q, France) and was used in all experiments. All chemicals were used as received and without further purification.

2.2. Preparation of the bacterial suspension

Firstly, the freeze-dried *S. pasteurii* stock was activated following the procedures outlined in the operating manual provided by CGMCC. After activation, the bacteria were inoculated onto solid NH_4-YE agar medium consisting of 20 g/L yeast extract, 10 g/L $(NH_4)_2SO_4$, 0.13 M Tris base, and 20 g/L agar, and then incubated at 30 ℃ for 48 h. Subsequently, several bacterial colonies from agar plates were picked and inoculated into liquid NH_4-YE medium (without agar). The inoculated medium was then incubated at 30 ℃ with a shaking speed of 200 r/min in a shaking incubator to obtain a bacterial suspension (BS) with an optical density at 600 nm (OD_{600}) of approximately 2.0. The NH_4-YE medium was firstly sterilized at 121 ℃ for 20 min using an autoclave before usage.

2.3. Preparation of the MICP-coated SSM

To prepare the mineralization solution (MS) for the formation of the MICP coating, urea and nutrient broth were dissolved into DI water and subsequently sterilized at 121 ℃ for 20 min using an autoclave. Following that, $CaCl_2{\cdot}2\ H_2O$ was chosen as the calcium source and was dissolved in the sterilized and cooled solution to obtain the mineralization solution. In this study, the mineralization solution contained equal molar concentrations of $CaCl_2{\cdot}2\ H_2O$ and urea, with the nutrient broth concentration maintained at 3 g/L. Three concentrations of $CaCl_2{\cdot}2\ H_2O$ were utilized: 0.05, 0.15, and 0.25 M. The initial pH values of the three concentrations of mineralization solutions were 8.08, 8.33, and 8.50, respectively. A piece of SSM with a size of 10 $\times$ 2 cm^2 was ultrasonically cleaned using anhydrous ethanol for 15 min, then dried at 60 ℃, and finally sterilized under ultraviolet light for 15 min on each side of the mesh. After that, the sterilized mesh was immersed in the mineralization solution. Subsequently, the bacterial suspension with an

optical density at 600 nm (OD_{600}) of approximately 2.0 were injected to the mineralization solution and then incubated in an incubator at a shaking speed of 150 r/min for 24 h. Three different final concentrations of the bacterial suspension were employed: 0.05×10^8, 0.1×10^8, and 0.2×10^8 cells/mL. In addition, the MICP process was investigated at three different temperatures (15, 25, and 35 ℃). The specific experimental conditions are detailed in Table 1 and 2. After immersing the meshes in the mineralization solution for 24 h, they were taken out and subsequently rinsed with DI water and anhydrous ethanol to eliminate any remaining organic matter and loose $CaCO_3$ particles. Finally, the obtained MICP-coated SSMs were dried at 60 ℃ in a drying oven. In this study, three parallel samples were prepared for each group.

2.4. Characterization

The surface morphologies of the MICP-coated SSMs were characterized via a Nova NanoSem450 scanning electron microscope (SEM). The elemental composition and the element distribution of the sample surfaces were characterized using an energy-dispersive spectrometer (EDS). The samples were sputter-coated with platinum before SEM testing. The X-ray diffraction (XRD) pattern of the MICP coatings was recorded on an X-ray diffractometer (Rigaku Smartlab, Japan) using a Cu Kα radiation, with 2θ in the range of 10–90° at a scan rate of 15°/min. The surface roughness of the samples was analyzed using a white light interferometer (Bruker Contour GT-1). The optical density at 600 nm (OD_{600}) of the *S. pasteurii* in the NH_4-YE medium was measured using an ultraviolet spectrophotometer (UV-6100S, Metash, China). The pH value of the mineralization solution was measured on a PB-10 pH meter (Sartorius, Germany). The wettability and oil adhesion behaviors of the meshes were tested at room temperature using a contact angle measuring instrument (SDC-100SH, Sindin, China). For static water contact angles (WCAs) in air, water droplets (5 μL) were directly dropped on the mesh. For underwater oil contact angles, the meshes were firstly fixed in a transparent quartz container filled with water, and then 10 μL oil droplets were carefully deposited on the mesh. The measurement procedure for the underwater oil rolling angles (UWORAs) was almost identical to that of the UWOCAs, with the exception that the quartz container, along with the meshes, was positioned on a tiltable platform. Angle measurements were taken at three distinct positions for each sample in order to calculate an average value. The oil concentration in the filtrate was determined using a water detective 3-multi parameter spectral water quality detector (WQM01H-3, China).

2.5. Durability and stability tests

The chemical stability of the MICP-coated SSMs was assessed by immersing them in aqueous media, including solutions with pH ranging from 1–14 and a 3.5 wt% NaCl solution, for a duration of 2 h. The thermal stability of the MICP-coated SSMs was evaluated by placing them in a muffle furnace at temperatures of 100 ℃, 200 ℃, and 300 ℃ for 2 h, respectively. The mechanical durability of the MICP-coated SSMs was examined using a sand impact method. In brief, a total of about 350 g of sand grains with diameters ranging from 0.5–1 mm were poured uniformly from a height of 20 cm onto the surfaces of the MICP-coated SSMs tilted at an angle of 30°. The sand impingement test was repeated 15 times. The contact angle, morphology, water flux, and oil rejection rate of the MICP-coated SSMs were investigated after the aforementioned tests.

Table 1
Experimental parameters with varying BS concentration and MS concentration.

No.	Temperature (℃)	Bacterial suspension concentration ($\times 10^8$ cells/mL)	Mineralization solution concentration (M)
A1	25	0.05	0.05
A2	25	0.1	0.05
A3	25	0.2	0.05
A4	25	0.05	0.15
A5	25	0.1	0.15
A6	25	0.2	0.15
A7	25	0.05	0.25
A8	25	0.1	0.25
A9	25	0.2	0.25

Table 2
Experimental parameters with varying temperatures.

No.	Temperature (℃)	Bacterial suspension concentration ($\times 10^8$ cells/mL)	Mineralization solution concentration (M)
B1	15	0.1	0.15
B2	25	0.1	0.15
B3	35	0.1	0.15

2.6. Measurement of water capture capability

To evaluate the water capture capability of the MICP-coated SSMs, the meshes were immersed in DI water for 10 min. Subsequently, the meshes were taken out from the water and weighed after no water droplets fell. The water capture percentage (WCP) was calculated as follows:

$$WCP = \left(\frac{w_2 - w_1}{w_1}\right) \times 100\% \quad (1)$$

herein, w_1 and w_2 represent the weight of the meshes before and after the water immersion tests, respectively.

2.7. Oil-water separation experiments

In this work, diesel, machine oil, soybean oil, hexane, petroleum ether, and dichloromethane were employed to assess the immiscible oil-water separation performance of the prepared MICP-coated SSM. One piece of prewetted MICP-coated SSM was fixed between two vertical quartz tubes using a clamp. The filtrate was collected in a beaker. The inner diameter of the quartz tube was 14 mm. Subsequently, an oil-water mixture with a volume ratio of 1:1 was poured into the upper quartz tube, and water rapidly permeated the MICP-coated SSM under gravity force. The separation process was repeated three times for each experiment. The filtration flux (F, L m^{-2} h^{-1}) was calculated using the following equation:

$$F = \frac{V}{A\Delta t} \quad (2)$$

herein, V (L) is volume of the filtrated water, A (m^2) is the effective filtration area of the MICP-coated SSMs, and Δt (h) is the filtration time. The oil rejection rate (η, %) was calculated using the following equation:

$$\eta = \left(1 - \frac{C_f}{C_o}\right) \times 100\% \quad (3)$$

herein, C_f and C_o are the concentration of oil in the filtrated water and the original mixtures, respectively. To investigate the stability of the MICP-coated SSM during the separation process, the procedure was repetitively performed for 40 consecutive cycles without any rinse treatment. After each separation of a 40 mL mixture, the filtrate was collected to evaluate the separation efficiency and water flux. The oil intrusion pressure was determined by gradually adding hexane into the upper quartz tube (length: 1 m) until the MICP-coated SSM could no longer sustain the pressure. The maximum height of the hexane was then recorded.

3. Results and discussion

3.1. Fabrication and morphologies comparison of MICP-coated SSMs

The preparation procedure of MICP-coated SSMs is illustrated in Fig. 1. The clean SSM was initially immersed in a mineralization solution containing $CaCl_2{\cdot}2\,H_2O$, urea, and nutrient broth. Following that, *S. pasteurii* bacteria were introduced to induce the formation of minerals on the SSM surface with the help of its urea hydrolytic ability. The basic mechanism of hydrolysis-driven MICP can be summarized by the following two reaction equations [49,50]:

$$CO(NH_2)_2 + 2H_2O \xrightarrow{urease} 2NH_4^+ + CO_3^{2-} \quad (4)$$

$$Ca^{2+} + CO_3^{2-} \rightarrow CaCO_3 \downarrow \quad (5)$$

MICP is a biochemical reaction process initiated by bacteria and culminating in an ionic reaction between calcium ions and carbonate. Firstly, the bacterial urease present in *S. pasteurii* bacteria can hydrolyze urea in the solution, producing ammonia and carbon dioxide, which will further react with water to form ammonium and carbonate ions (Eq. (4)). Subsequently, calcium ions in solution will be absorbed on the surface of the bacteria due to the negative charge on its surface. Finally, sufficient calcium ions will react with the carbonate and initiate calcium carbonate precipitation on the SSM surface using bacteria as nucleation sites (Eq. (5)). As shown in Fig. S1, it was evident that the originally silver-gray surface of the SSM underwent a transformation to a darker shade after mineral formation. Additionally, a significant amount of grayish-white minerals were observed coating the inner surface of the test tube. The EDS spectrum and elemental mapping images (Fig. S2a, b) indicate that the mineral-coated mesh mainly contained C, O, and Ca elements. The XRD pattern (Fig. S2c) further reveals that all sharp diffraction peaks can be assigned to $CaCO_3$ (JCPDS: 88–1807), except for substrate peaks. These results firmly confirmed the successful deposition of calcium carbonate precipitates on the SSM surface. It is noteworthy that the MICP process occured naturally, taking place at mild temperatures and in the air atmosphere without human intervation. Additionally, the MICP process would occur mildly and safely in the presence of the *S. pasteurii*. These advantages endow the MICP process with characteristics of being cost-effective, simple, easy to operate, and environmentally friendly.

The surface morphologies of the MICP-coated SSMs after incubation in various environmental factors were characterized by SEM, as shown in Fig. 2 and Fig. 3. Samples A1 and A2, incubated in a mineralization solution with a low concentration of calcium source and bacteria, exhibited relatively smooth surface characteristics upon observation. The surfaces of samples A1 and A2 showed no regular calcium carbonate crystal structures, and the mesh aperture remained at approximately 25 μm (Fig. 2a, b and S3a, b). At a BS concentration of 0.2×10^8 cells/mL, numerous randomly distributed fine $CaCO_3$ crystals started to appear on the surface of sample A3 (Fig. 2c and S3c). When the MS concentration reached 0.15 M, a dense and continuous $CaCO_3$ layer was observed on the SSM surface (Fig. 2d-f and S3d-f). This confirmed that by optimizing the MS concentration, a dense mineral layer could be formed on the mesh surface within 24 hours, which was a great improvement over previous works [47,48]. Here, we conducted an analysis of crystal size in the SEM images using ImageJ software. As shown in Fig. S4, the crystal sizes on the surface of samples A4, A5, and A6 were mainly in the ranges of 10–40 μm, 5–30 μm, and 5–15 μm, respectively. It should be noted that although the $CaCO_3$ crystal size became smaller, the pore size of the meshes decreased with the increase of BS concentration, and the aperture decreased from an average of 14.9 μm (sample A3) to an average of 3.4 μm (sample A5). By increasing the MS concentration to 0.25 M, additional tiny $CaCO_3$ particles were deposited onto the previously-generated crystals (Fig. 2g-i and S3g-i), leading to the pores of the SSM being almost blocked.

Fig. 3 shows the effect of temperature on the morphology of $CaCO_3$ crystals on the SSM surface. Elevated temperatures from 15 ℃ to 35 ℃ facilitated the generation of a greater number of $CaCO_3$ precipitates, consequently causing a gradual reduction in the pore size of the mesh (Fig. 3a and b). Ultimately, the pores approached a state of near blockage due to the increased formation of $CaCO_3$ deposits (Fig. 3c). In the MICP process, higher temperature could facilitate the hydrolysis of urea, resulting in the production of more carbonate ions. Consequently, the reaction reached oversaturation more quickly, thereby accelerating crystal growth rate [51,52].

3.2. Surface wettability of MICP-coated SSMs

In order to evaluate the influence of environmental factors on the wettability of MICP-coated SSMs, the dynamic water wetting process and UWOCAs were measured. It is well known that the attainment of superhydrophilicity and underwater superoleophobicity relies on two fundamental principles: a surface chemical composition with high surface energy and a rough surface structure [25]. The initial WCA of the original SSM was 126.7° (Fig. S5a), attributed to the presence of highly dense mesh that could potentially trap a small amount of air. However,

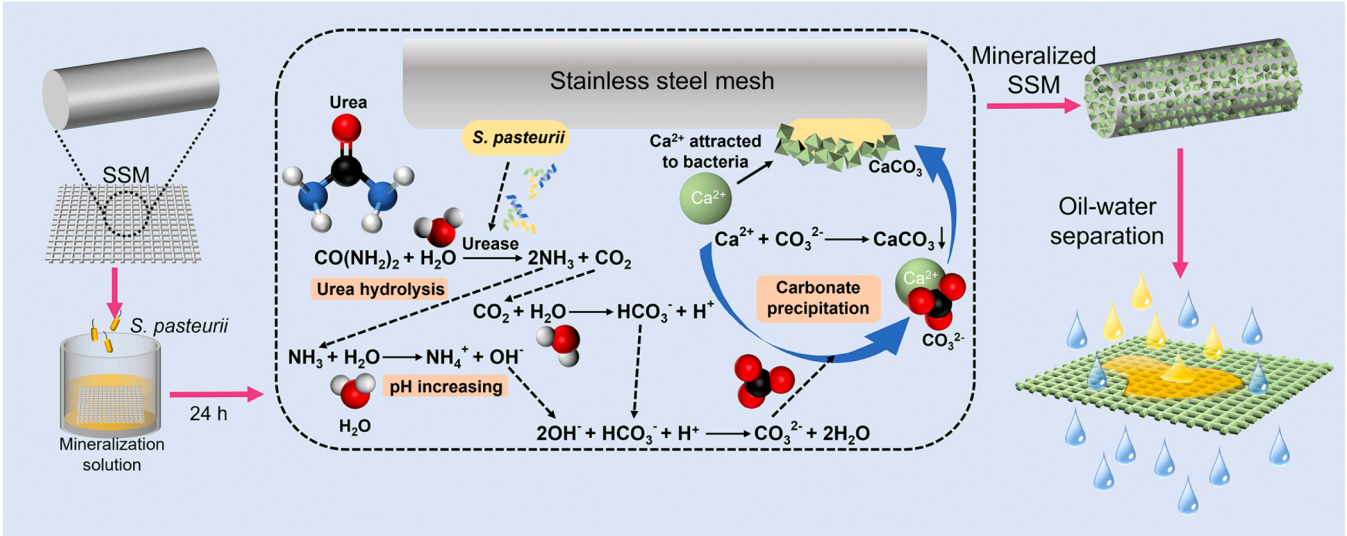

Fig. 1. Schematic of the microbial-induced calcium carbonate precipitation process and the oil-water separation process.

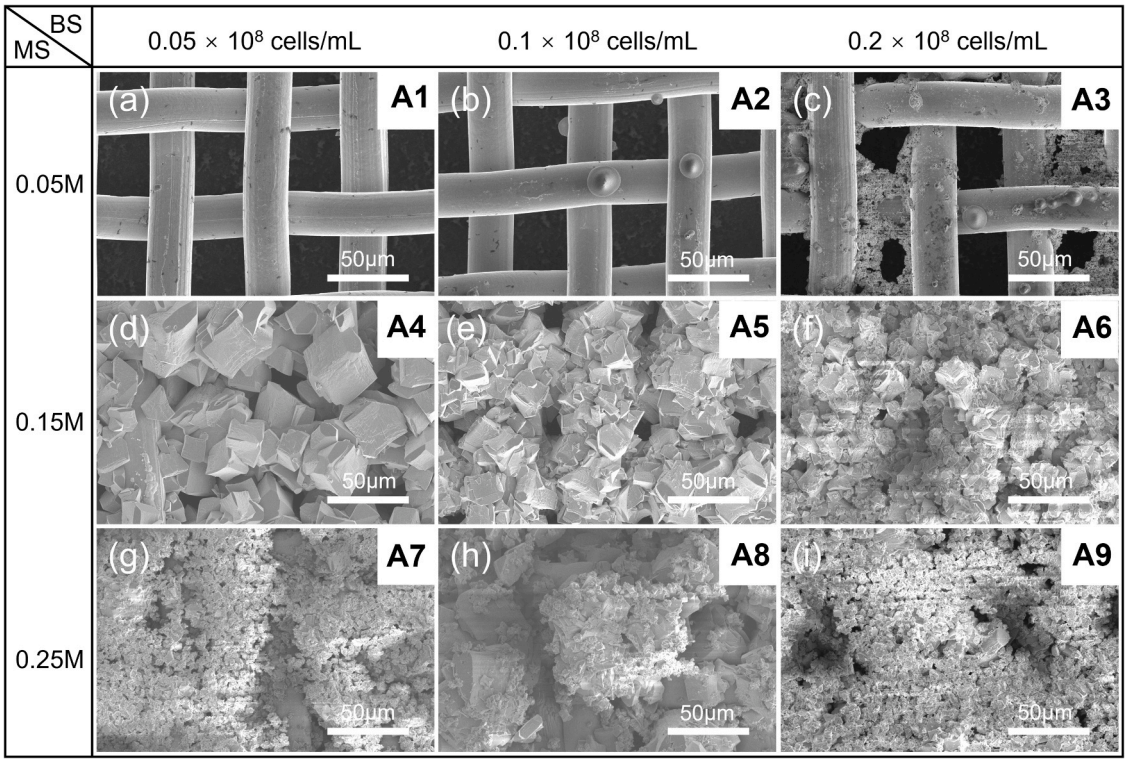

Fig. 2. SEM images of MICP-coated SSMs with different BS and MS concentrations at 25 ℃.

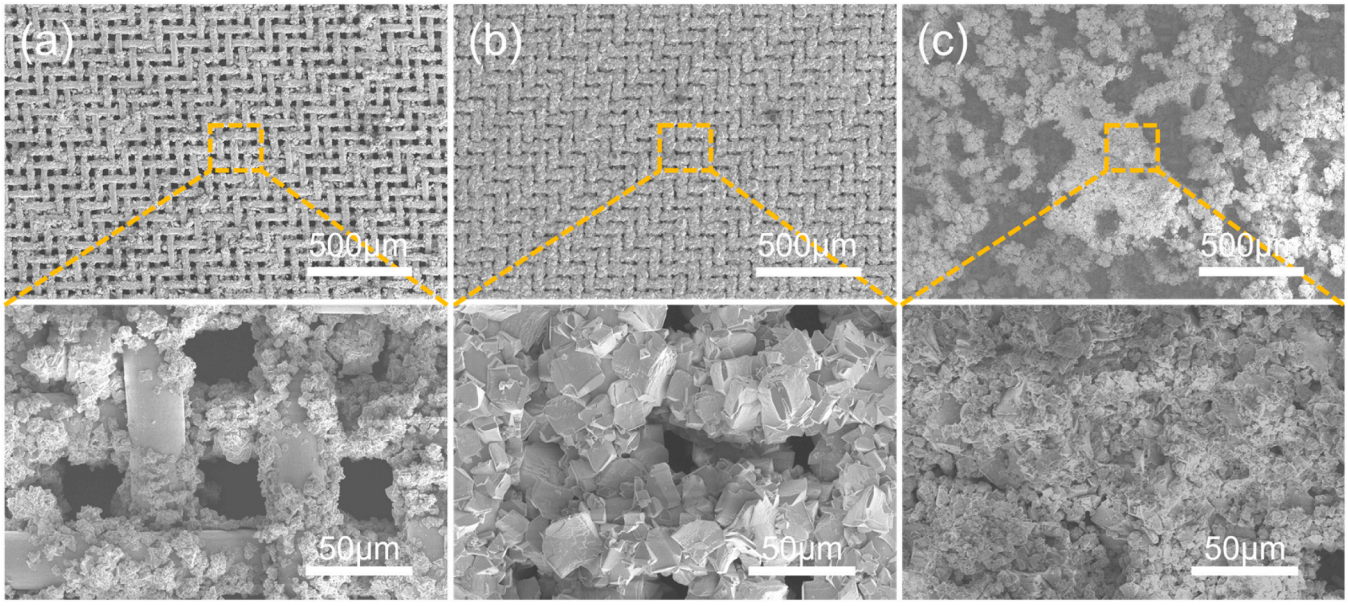

Fig. 3. SEM images of MICP-coated SSMs at different temperatures with a BS concentration of 0.1 × 10^8 cells/mL and an MS concentration of 0.15 M: (a) 15 ℃; (b) 25 ℃; (c) 35 ℃.

the water wetting property exhibited significant reinforcement upon the formation of micro/nanostructured MICP coatings. As shown in Fig. 4a, the WCAs of samples A1 and A2 decreased to 73.3° and 67.1° within one minute, respectively, showing hydrophilicity. Upon increasing the BS concentration to 0.2 × 10^8 cells/mL (sample A3), it was observed that a 5 μL water droplet could completely spread on the surface of the MICP-coated SSM in air, reaching a WCA of 0° within 7.548 s. The observed result confirmed the superhydrophilic ability of the MICP-coated SSM (sample A3), attributed to the formation of a small amount of $CaCO_3$ particles on the surface of the SSM (Fig. 2c). During this period, the average surface roughness (R_a) of A3 exhibited a slight increase, approximately 8% higher compared to A2, reaching 0.401 μm. In addition, with a further increase in the MS concentration, the water wettability was further enhanced. Upon water droplets dropping on the surface of the MICP-coated SSMs, it rapidly spread on the meshes within one second (Fig. 4a: samples A4-A9). It is worth noting that the MS concentration has a greater effect on the water wettability of the MICP-coated SSM compared to the BS concentration. As shown in

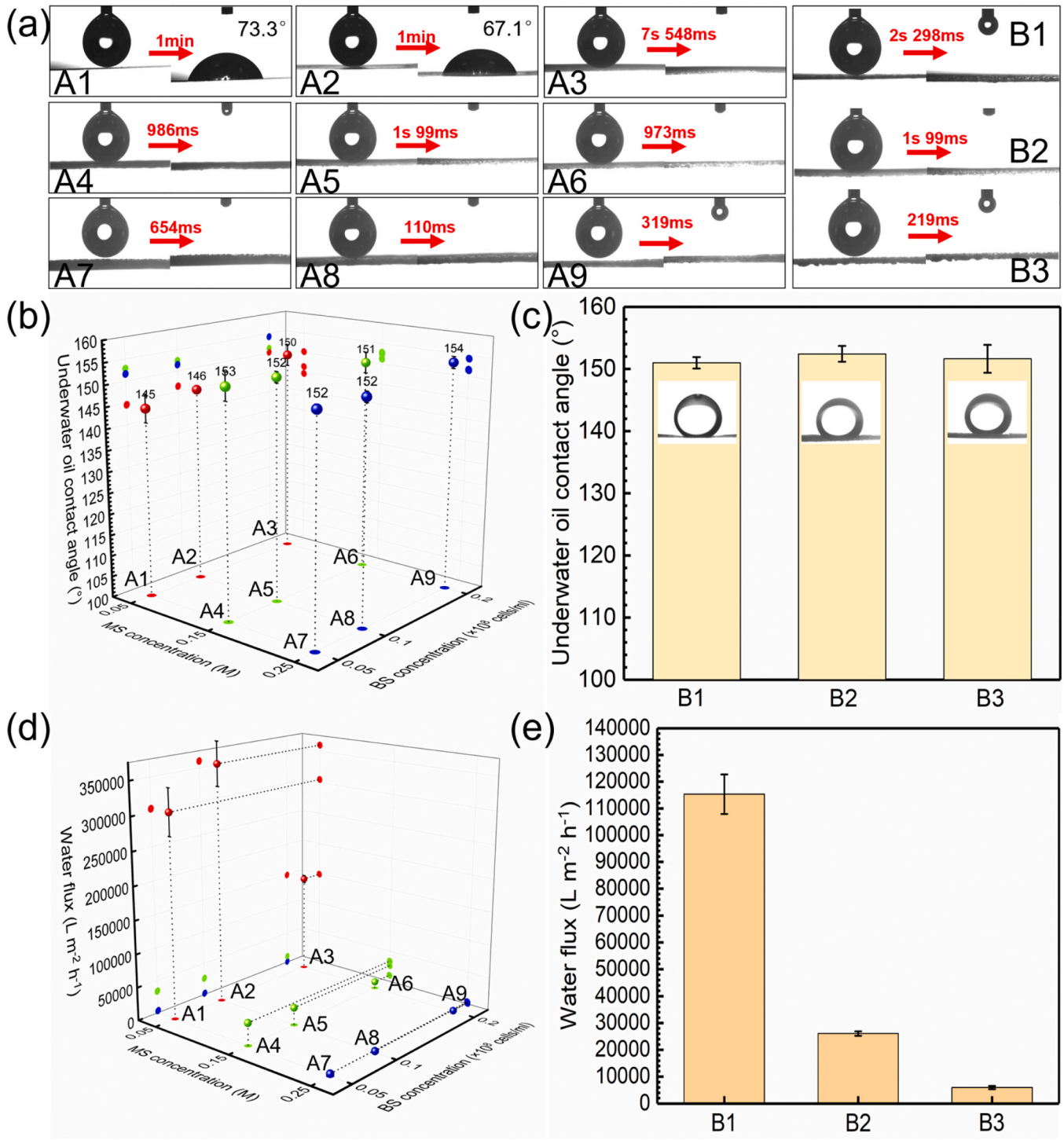

Fig. 4. (a) Dynamic wetting process of water droplets on the surface of MICP-coated SSMs. UWOCAs of (b) samples A1-A9 and (c) samples B1-B3. Water flux of (d) samples A1-A9 and (e) samples B1-B3.

Fig. 4a, there was a notable decrease in the time required for complete surface wetting as the MS concentration increased. This phenomenon could be primarily attributed to the presence of smaller and denser $CaCO_3$ particles (Fig. 2d-i), as well as an increase in surface roughness. As shown in Fig. S6, the R_a of the samples increased obviously with increasing MS concentration. When the MS concentration was 0.15 M, the increase in BS concentration had little effect on the surface roughness (sample A4-A6 was 0.509 μm, 0.548 μm, and 0.575 μm, respectively). However, as the MS concentration reached 0.25 M and the BS concentration was greater than or equal to 0.1×10^8 cells/mL (sample A8), a significant increase in surface roughness was observed compared to sample A7. Given that samples A8 and A9 exhibited the highest R_a, measuring 0.928 μm and 0.923 μm, respectively, water droplets could completely wet the mesh surface in the shortest time - approximately 110 ms for A8 and about 319 ms for A9 (Fig. 4a). This was primarily due to the formation of numerous smaller calcium carbonate particles on the surface of the original cubic calcium carbonate particles (Fig. 2h). As shown in Fig. S3h, as the BS concentration continued to increase, more calcium carbonate particles were formed and stacked on the surface of the mineralized steel mesh, creating numerous protruding structures.

Consequently, a thicker calcium carbonate layer was formed on the mesh surface (Fig. S3i). Furthermore, the water wettability of the MICP-coated SSM surface was positively correlated with temperature. The time required for water droplets to completely wet the mesh surface decreased significantly from 2.298 s at 15 °C to 219 ms at 35 °C, as shown in Fig. 4a: B1-B3.

To explore the underwater oleophobic property, a 10 μL droplet of DCM was utilized to measure the UWOCAs of various MICP-coated SSMs. The UWOCAs of samples A1 and A2 (Fig. 4b) exhibited consistency with the original SSM (Fig. S5b), as both being below 150°. However, when the MS concentration exceeded 0.05 M, the UWOCAs of samples A4 to A9 were all higher than 150° (Fig. 4b), showing underwater superoleophobicity. Furthermore, the UWOCAs of samples B1, B2, and B3 were also measured to be higher than 150° (Fig. 4c). Upon immersing the MICP-coated SSMs of samples A3 to A9 and B1 to B3 in water, water hydrates formed on the micro/nano-structures due to the intrinsic hydrophilicity of $CaCO_3$. The water hydration layer effectively acted as a barrier, preventing direct contact between oil droplets and the mesh surface. As a result, the MICP-coated SSMs exhibited a high UWOCA. According to Jiang et al.'s model [24], the high UWOCA on the solid surface can be analyzed by following equation:

$$\cos\theta_3 = \frac{\gamma_{oa}\cos\theta_1 - \gamma_{wa}\cos\theta_2}{\gamma_{ow}} \tag{6}$$

where γ_{oa} is the oil-air interface tension, θ_1 is the contact angle of oil in air, γ_{wa} is the water-air interface tension, θ_2 is the WCA in air, and γ_{ow} is the oi-water interface tension. Generally, the values of γ_{oa} range from 20 to 30 mN m^{-1}, while the value of γ_{wa} is 73 mN m^{-1}. Due to the near-zero value of θ_1 and the constant interfacial tension of various oils, a decrease in θ_2 leads to an increase in θ_3. In other words, a surface that is more hydrophilic exhibits more oleophobic when submerged in water. After the MICP process, a hydrophilic $CaCO_3$ layer formed, leading to a significant decrease in θ_2 and a substantial increase in θ_3. The UWOCAs of the $MICP_{(A5)}$-coated SSM were also measured for various oils. As demonstrated in Fig. S7, the UWOCAs of the $MICP_{(A5)}$-coated SSM towards all tested oils exceed 150°, indicating excellent underwater superoleophobicity. In contrast, pristine SSM showed weak oleophobicity, with UWOCAs below 150° for various oils. The UWORA is also another crucial parameter for evaluating underwater superoleophobicity. As shown in Fig. S8, the UWORAs of samples A3-A9 and B1-B3 were all below 5°, indicating that DCM droplets could easily roll off these surfaces. However, DCM droplets failed to roll off on the surface of original SSM and samples A1, A2, and even when the tilted angle exceed 10° (Fig. S5c, d and S8).

The water fluxes of the MICP-coated SSMs were determined by both their pore sizes and wettability, which were directly related to the density and particle size of the $CaCO_3$ particles. Notably, the pore sizes played a predominant role because all the MICP-coated SSMs, except samples A1 and A2, exhibited superhydrophilicity. As shown in Fig. 4d, since there were no $CaCO_3$ layers on the mesh surface, samples A1 and A2 exhibited the highest water fluxes among the tested samples (304,880 L m^{-2} h^{-1} for A1, 359,993 L m^{-2} h^{-1} for A2). When the MS concentration reached 0.15 M or higher, a significant decrease in water flux was observed. Specifically, the water fluxes for samples A4 to A9 decreased to 33,555, 26,080, 10,039, 3186, 1960, and 859 L m^{-2} h^{-1}, respectively. This confirmed that the pore size of the SSM decreased with the increase of BS and MS concentration, as proved by the SEM results. Furthermore, Fig. 4e confirmed that an increase in temperature indirectly led to a decrease in the water flux of the MICP-coated SSMs, which were 115,335, 26,080, and 5967 L m^{-2} h^{-1} for samples B1, B2, and B3, respectively.

3.3. The oil intrusion pressure on MICP-coated SSMs

The porous mesh and membrane materials demonstrate diametrically opposite permeability characteristics towards water and oil, forming the fundamental principle for oil-water separation. The intrusion pressure, which is closely associated with wettability and pore size, plays a crucial role in gravity-driven oil-water separation processes [25, 53]. In theory, the intrusion pressure (Δp) is calculated by the following equation [54,55]:

$$\Delta p = \frac{2\gamma_{ow}}{R} = -C\gamma_{ow}\frac{\cos\theta_a}{A} \tag{7}$$

where γ_{ow} is the oil-water interfacial tension, R is the radius of the meniscus, C is the circumference of the pore, θ_a is the advancing contact angle, and A is the area of the pore. As shown in Fig. 5a and b, the superhydrophilic MICP-coated SSM exhibited a very low θ_a, approaching 0°, which led to a negative Δp when in contact with water. This indicated that the MICP-coated SSM was unable to withstand any pressure exerted by water under the capillary effect and gravity, allowing water to pass through the mesh smoothly. Consequently, as the water completely wrapped the intrinsic hydrophilic micro/nano-structured $CaCO_3$ coatings adhered to the mesh surface (Fig. 5c), a stable water film was formed, significantly enhancing the oil repellency of the mesh surface and leading to its superoleophobic behavior. When the oil contacted the water film on the mesh, the Δp changed to positive as the θ_a was much larger than 90° (Fig. 5d). Therefore, as long as the hydrostatic pressure of the oil does not exceed the maximum intrusion pressure value, the oil cannot pass through the MICP-coated SSM. However, once the static pressure (p) of the oil surpasses this critical value of Δp, it can still penetrate through the mesh pores. Therefore, the experimental static pressure (p) was also determined by measuring the maximum height (h_{max}) of oil that the pre-wetted MICP-coated SSMs could withstand. The value of p was calculated using following equation:

$$p = \rho g h \tag{8}$$

where ρ is the density of the oil, g is the acceleration of gravity, and h is the height of the oil. As shown in Fig. 5e and S9, samples A1 and A2 were unable to support any oil pressure, and no hexane was observed in the upper tube (Fig. S9). However, when the BS concentration reached 0.2×10^8 cells/mL (sample A3), the formation of a small amount of $CaCO_3$ particles on the surface of the SSM enhanced the water wettability of the mesh to a certain extent. Consequently, sample A3 exhibited a slight oil pressure tolerance, allowing for a maximum height of hexane reaching 4 cm, indicating that the p reached the Δp. With the increase of MS concentration to 0.15 M and above, the height of hexane surpassed 47 cm, accompanied by a p exceeding 3 kPa, which demonstrated the excellent oil pressure tolerance of these pre-wetted MICP-coated SSMs (samples A4-A9). Due to the much smaller pore sizes of samples A4-A9 compared to sample A3 (Fig. 2), the intrusion pressure would be significantly larger for the former, according to Eq. (7). Similarly, an elevation in temperature would correspondingly lead to an augmentation in the value of p. As displayed in Fig. 5f, the p of hexane on samples B1, B2, and B3 calculated 1.72, 3.08, and 3.43 kPa, respectively. Moreover, the static pressure tolerance of the prepared meshes was found to be higher than the reported values, as shown in Table 3.

Supplementary material related to this article can be found online at doi:10.1016/j.jece.2023.111805.

Supplementary material related to this article can be found online at doi:10.1016/j.jece.2023.111805.

Supplementary material related to this article can be found online at doi:10.1016/j.jece.2023.111805.

3.4. Oil-water separation performance

Based on the discussion of the section 3.2 and 3.3, sample A5, obtained at a BS concentration of 0.1×10^8 cells/mL and an MS concentration of 0.15 M, demonstrated higher water flux compared to sample A8, while exhibiting better hydrostatic pressure performance than

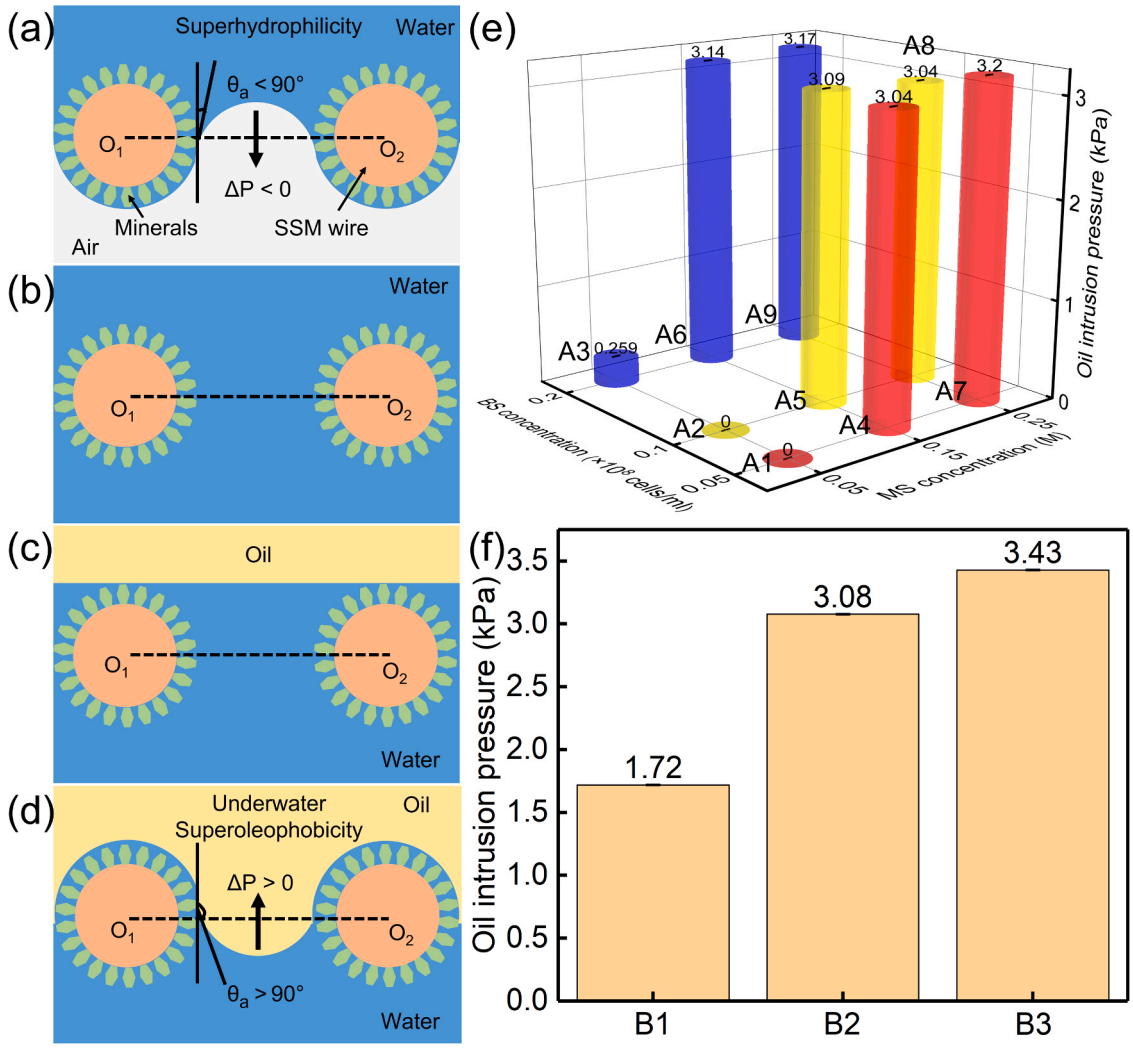

Fig. 5. (a-d) Schematic diagrams of the oil-water separation process. (e) Intrusion pressure of hexane on (e) samples A1-A9 and (f) samples B1-B3.

Table 3
Oil-water separation performance Comparison of $MICP_{(A5)}$-coated SSM with the previous metal mesh-based materials.

Materials	Highest intrusion pressure (kPa)	Highest flux (L m^{-2} h^{-1})	Efficiency (%)	Refs.
Multi-scale CuBTC-coated mesh	2.2	533,880	> 99	[26]
NaA zeolite/copper mesh	1.14	10,114	98.6	[30]
GO-$CaCO_3$-5_{20} hybrid mesh	1.37	179,640	> 99	[38]
ZnO/WO_3·H_2O coated SSM	1.36	34,387	> 98	[56]
CuO@PAA composite coated copper mesh	-	6460	> 99.9	[57]
$NiCo_2O_4$ structure coated SSM	-	11,600	> 99.9	[58]
Bicomponent supramolecular hydrogel paint coated SSM	-	10,000	> 99	[59]
PMAA-grafted mesh	1.99	50,000	> 99	[60]
Annealed SSM	-	6098	99.5	[61]
$MICP_{(A5)}$-coated SSM	3.08	28,644	> 99.9	This work

sample A2. Moreover, sample A5 exhibited higher water flux than A6, with slightly superior hydrostatic pressure compared to A4. Additionally, it was observed that the water flux of sample B2 (equivalent to A5) exceeded that of sample B3, while its hydrostatic pressure was superior to sample B1. Consequently, sample A5 was identified as the best candidate for high-performance oil-water separation and was used for subsequent experiments. The prewetted $MICP_{(A5)}$-coated SSM was positioned between two vertical fixed quartz tubes using a clamp. As shown in Fig. 6a and Movie S1, when the hexane-water mixture was poured into the upper tube, it was clearly found that only water rapidly penetrated through the $MICP_{(A5)}$-coated SSM and was collected in the beaker below, while the hexane was effectively blocked and retained trapped in the upper tube. By contrast, the original SSM failed to separate the hexane-water mixture, as shown in Fig. 6a and Movie S2. For heavy oil ($\rho_{oil} > \rho_{water}$), such as dichloromethane, we can tilt the separation device at a certain angle and pour the mixture slowly to prevent the heavy oil from blocking the penetration of water (Fig. S10).

Supplementary material related to this article can be found online at doi:10.1016/j.jece.2023.111805.

Fig. 6b shows the separation flux and the oil rejection rate of the $MICP_{(A5)}$-coated SSM for various oil-water mixtures. The separation flux of the $MICP_{(A5)}$-coated SSM for petroleum ether-water mixture reached up to 28,644 L m^{-2} h^{-1}, whereas for the soybean oil-water mixture, it was relatively low but still exceeded 10,942 L m^{-2} h^{-1}, which is superior to most similar mesh materials (see Table 3). The variation in

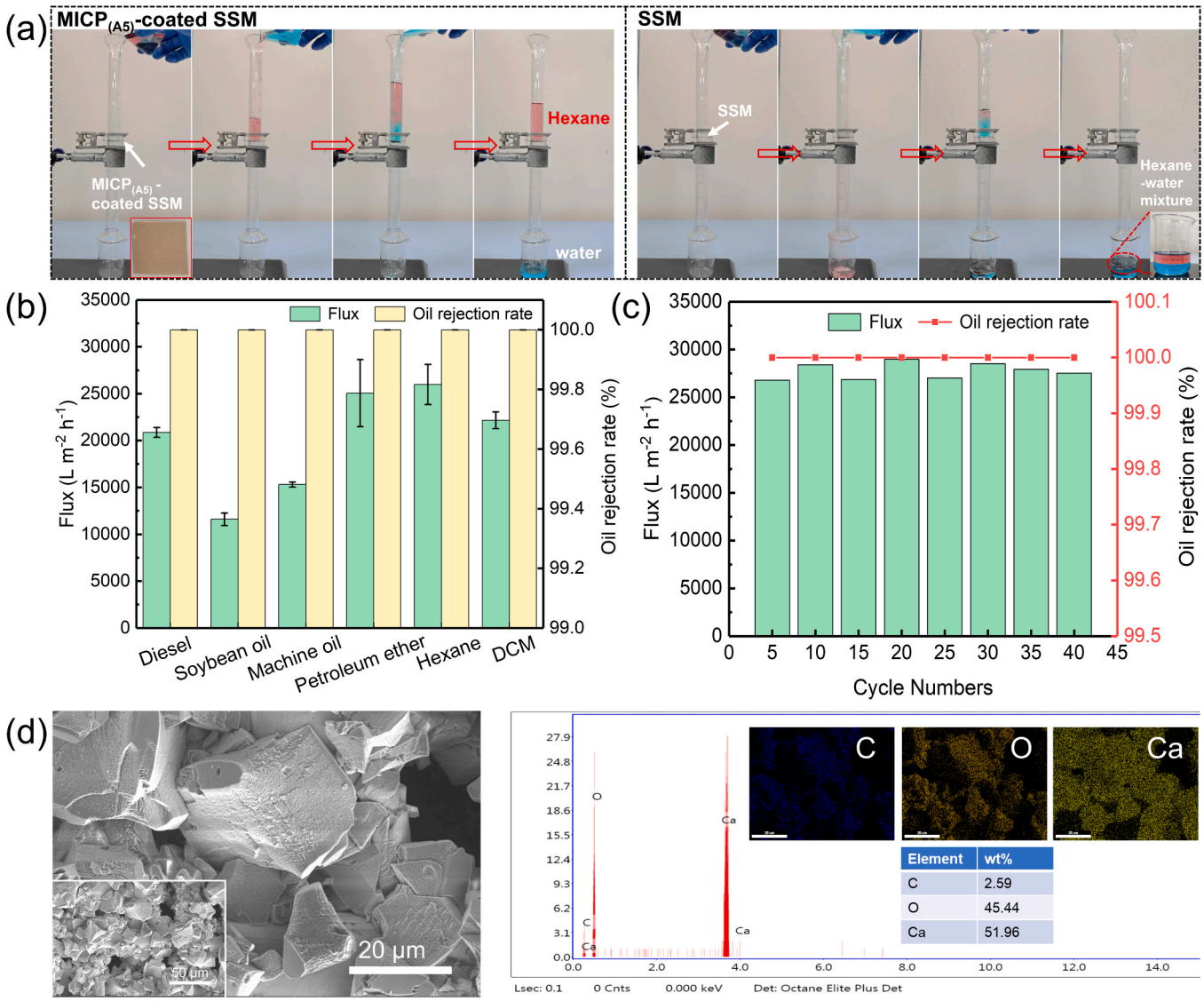

Fig. 6. (a) The oil-water separation process of the MICP$_{(A5)}$-coated SSM (left) and original SSM (right). (b) Flux and oil rejection rate of the MICP$_{(A5)}$-coated SSM for different oil-water mixtures. (c) The changes in flux and oil rejection rate of the MICP$_{(A5)}$-coated SSM after 40 consecutive separations using a hexane-water mixture as an example. (d) SEM images of the MICP$_{(A5)}$-coated SSM after 40 cycles of use and the corresponding EDS spectrum and elemental mapping images.

separation flux for different oil-water mixtures directly correlated with the density and viscosity of the tested oils [28]. High-viscosity oils impeded the sediment of water and resulted in decreased water flux during the separation process. This phenomenon could be further demonstrated by the Stokes theorem, the formula is as follows:

$$v = \frac{d^2 \quad g(\rho_w - \rho_o)}{18\mu_w} \tag{9}$$

where v represents the velocity of oil droplets, d denotes the diameter of oil droplets, g is the acceleration of gravity, ρ_w and ρ_o are the density of water and oil, respectively, and μ_w is the viscosity of water [62]. According to Eq. (9), a greater density difference between water and oil results in faster oil droplet rise in water, thereby increasing water flux during the separation process. Hence, the order of water flux in the separation process for various oil-water mixture systems was as follows: petroleum ether-water/hexane-water > diesel-water > machine oil-water > soybean oil-water. The densities of the oils are as follows: petroleum ether (ρ: 0.66 g/mL), hexane (ρ: 0.659 g/mL), diesel (ρ: 0.83–0.85 g/mL), machine oil (ρ: 0.89 g/mL), and soybean oil (ρ: 0.917 g/mL). In this study, the speed at which the DCM-water mixture was poured into the upper tube was artificially interfered, so it will not be discussed here. As shown in Fig. 6b, the MICP$_{(A5)}$-coated SSM demonstrated excellent oil rejection performance, with an oil rejection rate exceeding 99.99% for all types of oils. This remarkable performance surpasses the values reported in the previous reports, as illustrated in Table 3. Additionally, the reusability of the MICP-coated SSMs is a crucial factor to consider for their practical application. Fig. 6c demonstrates that the flux of the MICP$_{(A5)}$-coated SSM remained relatively high (~ 27,533 L m^{-2} h^{-1}) with minimal variation even after 40 cycles of separation. The oil rejection rate of the MICP$_{(A5)}$-coated SSM remained above 99.99% throughout the 40 cycles of separation. Meanwhile, all $CaCO_3$ cubic structures were still covered on the SSM surface and the EDS spectrum (Fig. 6d) indicated that the weight percentages of C, O, and Ca elements remained almost the same as those before 40 cycles of separation (Fig. S2b). These results demonstrate the outstanding reusability of the MICP$_{(A5)}$-coated SSM.

In addition, the separation performance of oil-in-water emulsion was also evaluated, as shown in Fig. S11. We regretfully found that neither MICP$_{(A5)}$-coated SSM nor extending its mineralization time to 48 h (Fig. S11a) or increasing the concentration of the mineralization solution (MICP$_{(A9)}$-coated SSM, Fig. S11b) could effectively separate the

emulsion. As is known, filtration systems with pore sizes smaller than that of the emulsified oil droplets are commonly explored for emulsion separation applications. The pore sizes of the MICP-coated SSM were relatively larger than the size of oil droplets typically in the range of several hundred nanometers, making it unsuitable for separating the oil-in-water emulsions. Theoretically, increasing the thickness of the $CaCO_3$ coating by prolonging the mineralization time or increasing the concentration of the mineralization solution may lead to a decrease in the pore size of the SSM. However, both approaches led to partial detachment of the calcium carbonate layer from the steel mesh surface (Fig. S11 c and d), which contradicted the intended goal of reducing the pore size of the mesh. This part of the work requires further research in the future.

3.5. Anti-oil-fouling performance

The anti-oil-fouling performance is critical for efficient separation of oil-water mixtures. Fig. 7a showed the contacting and detaching processes of underwater DCM droplets onto the $MICP_{(A5)}$-coated SSM surface. After immersing the $MICP_{(A5)}$-coated SSM in water, a droplet of DCM was pressed onto the surface of the mesh until deformation occurred, and then it was dragged a certain distance before being lifted. During the retracting process, the DCM droplet easily detached from the mesh surface, and minimal deformation of the oil droplet was observed. This behavior highlighted the low adhesion and exceptional oil repellency properties of the mesh. On the contrary, a large deformation occurred during the retracting process, and the oil droplet tightly adhered to the surface of pristine SSM (Fig. S12). The excellent anti-oil-fouling property of the $MICP_{(A5)}$-coated SSM was further validated through various oil-repellence tests, depicted in Fig. 7b-d. Fig. 7b (black dashed outline, Movie S3) showed that the DCM droplet rapidly rolled off the tilted $MICP_{(A5)}$-coated SSM underwater. Moreover, when the $MICP_{(A5)}$-coated SSM was submerged in water, the expelled hexane flow rebounded from the surface without leaving any residual traces, as demonstrated in Fig. 7c (highlighted by the black dashed outline) and Movie S4. Furthermore, we investigated the anti-oil-fouling performance of the mesh under intrusion pressure. This was carried out by fixing the $MICP_{(A5)}$-coated SSM in the separation device, followed by pouring a certain amount of n-hexane (dyed red with oil red O) into the tube and let it sit for a period of time. Then we took out the mesh and found that no residue of red hexane was observed on the mesh surface. After the experiment, the mesh maintained its original dark gray color, as shown in Fig. S13. This demonstrated that even when subjected to a certain level of oil intrusion pressure, the $MICP_{(A5)}$-coated SSM maintained excellent oil repellency. As shown in Fig. 7d and demonstrated in Movie S5, the pre-wetted $MICP_{(A5)}$-coated SSM, previously adhered with hexane in air, exhibited a self-cleaning effect when immersed in water. These findings confirmed the outstanding anti-oil-fouling capability exhibited by the $MICP_{(A5)}$-coated SSM. In contrast, regardless of whether the oils were dropped onto the surface underwater or cleaned by immersing the mesh in water, they exhibited strong adhesion to pristine SSM (Fig. 7b-d, and Movies S6-S8). The presence of a strongly water film on the $MICP_{(A5)}$-coated SSM surface, which effectively prevented oil adhesion, was believed to be the primary factor contributing to its excellent oil repellence [63-65]. As shown in Fig. 7e, due to the relatively smooth surface of the original SSM, a stable hydration layer cannot be effectively formed. As a result, oil droplets may directly contact the surface of the mesh, leading to their adhesion. In contrast,

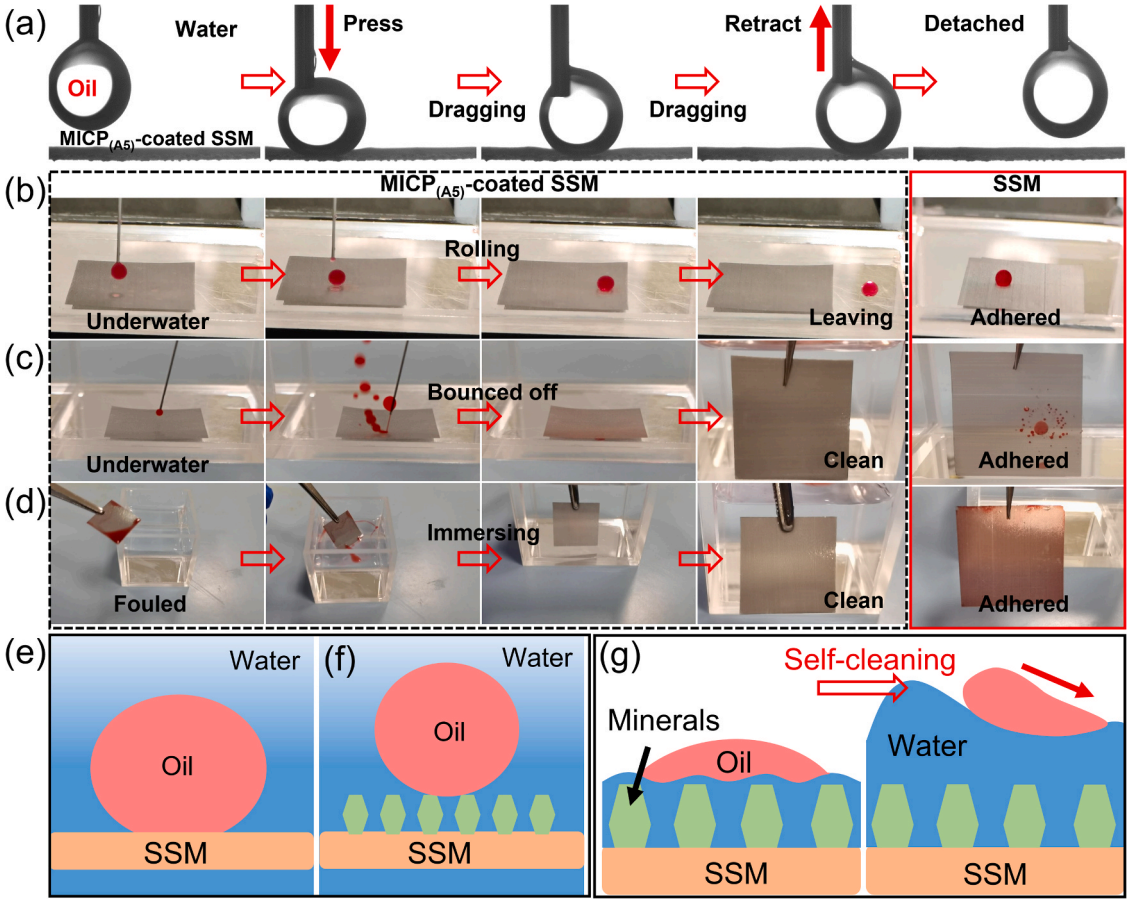

Fig. 7. (a) Underwater oil repelling behavior of the $MICP_{(A5)}$-coated SSM. (b, c) Anti-oil-fouling and (d) self-cleaning properties of the $MICP_{(A5)}$-coated SSM (black dashed outline) and the SSM (red solid outline). Schematic diagrams of the (e, f) anti-oil-fouling and the (g) self-cleaning mechanism. For better observation, oil was dyed red using oil red O.

the presence of numerous micro/nanoscale grooves, formed by the stacking of cubic superhydrophilic $CaCO_3$ particles, enabled the trapping of water molecules within the micro/nanostructures (Fig. 7f). This resulted in the formation of a stable water film that exhibited a strong repulsive effect on oils to prevent the oil from contacting the actual mesh surface. After the oil-contaminated pre-wetted mesh was immersed in water, the water film was reinforced, effectively washing away the oil from the surface, as shown in Fig. 7g. To demonstrate the effect of the water film on the anti-oil-fouling performance of the MICP-coated SSMs, water capture experiments were performed. As shown in Fig. S14, the water capture percentage of samples A4 to A9, which exhibited dense and continuous $CaCO_3$ layers, exceeded 32%, while the SSM, samples A1, A2, and A3 had lower percentages (18.2%, 18.6%, 19.2%, and 25.2% respectively). Accordingly, the presence of the intrinsic hydrophilic $CaCO_3$ layer facilitated the formation of a stable water film on the surface of the MICP-coated SSMs.

3.6. *Durability and stability of the MICP$_{(A5)}$-coated SSM*

The chemical, mechanical, and thermal stabilities of the mesh are

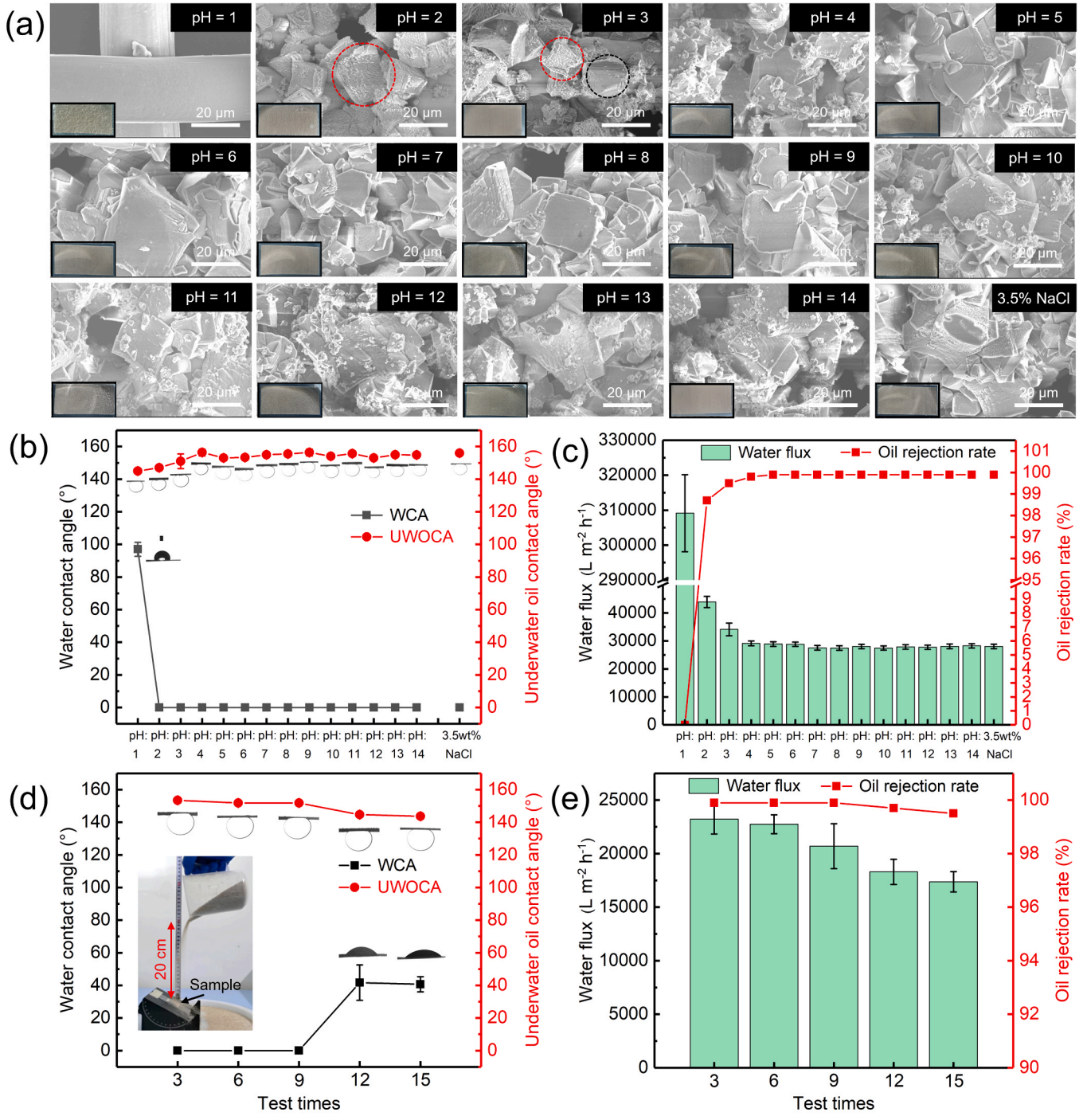

Fig. 8. The chemical and mechanical stability of MICP$_{(A5)}$-coated SSM: (a) SEM images and photos of the MICP$_{(A5)}$-coated SSM after a 2-hour immersion in solutions of various pH values and a 3.5 wt% NaCl concentration. (b) The corresponding WCA and UWOCA (the type of oil was petroleum ether). (c) Water flux and oil rejection rates of the MICP$_{(A5)}$-coated SSM after the immersion test. (d) WCAs, UWOCAs, as well as (e) water fluxes and oil rejection rates of the MICP$_{(A5)}$-coated SSM after sand impingement tests as a function of test times. Insets in (d) show the testing process.

crucial for its practical application in oil/water separation. Therefore, the stability of the $MICP_{(A5)}$-coated SSM was first evaluated under various harsh chemical environments, including exposure to salt (3.5 wt % NaCl), acid (HCl), and alkali (NaOH) solutions. The morphology of $MICP_{(A5)}$-coated SSM after a 2-hour immersion test was investigated. As shown in Fig. 8a, at pH= 1, almost no cubic $CaCO_3$ particles were observed on the surface of the mesh. At pH values of 2–3, the initially smooth surface of $CaCO_3$ (highlighted by the black circle) particles became rough (red circle), forming numerous burr structures, with partially exposed SSM visible. Additionally, it was observed that lots of bubbles formed on the mesh surface at pH=1 (insets in Fig. 8a). This was a result of the vigorous reaction between $CaCO_3$ and HCl. As the pH value increased to 2, the number of bubbles significantly decreased. Further raising the pH value to 3 resulted in almost no observable bubbles, indicating a significant reduction in the intensity of the reaction. In contrast, the cubic $CaCO_3$ microstructures were well maintained in pH solutions ranging from 4 to 14 and a 3.5 wt% NaCl solution, with no exposed SSM observed. The WCAs in air and UWOCAs are illustrated in Fig. 8b (the oil used here was petroleum ether), indicating that the $MICP_{(A5)}$-coated SSM maintained superhydrophilicity and underwater superoleophobicity at pH $\geq$ 3 and in a 3.5 wt% NaCl solution. Furthermore, the $MICP_{(A5)}$-coated SSM showed high water flux (up to 43937 L m^{-2} h^{-1}) and ultra-high oil rejection rate (> 98.7%) for petroleum ether-water mixtures after immersion in solutions with pH values higher than 2 and a 3.5 wt% NaCl solution (Fig. 8c), suggesting excellent chemical stability. However, after immersion in a solution with a pH of 1, the $MICP_{(A5)}$-coated SSM lost its ability to effectively separate oil and water.

The mechanical durability of the $MICP_{(A5)}$-coated SSM was investigated by the sand impingement test. The $MICP_{(A5)}$-coated SSM was initially fixed to an inclined surface with an inclination angle of 30°. Approximately 350 g of sand grains with diameters ranging from 0.5–1 mm were then uniformly poured from a height of 20 cm, impacting the surface of the mesh (insets in Fig. 8d). This test was repeated 15 times. As shown in Fig. 8d, after about 9 rounds of sand impingement tests, the $MICP_{(A5)}$-coated SSM still maintained superhydrophilicity and underwater superoleophobicity with a WCA of 0° and a UWOCA greater than 150°. However, after approximately 12 rounds of testing, the hydrophilicity of the $MICP_{(A5)}$-coated SSM surface significantly decreased, with the WCA increasing to 42° and the UWOCA decreasing to 145°. Fig. 8e shows that the water fluxes and oil rejection rates of the mesh gradually decreased with increasing testing times. It was observed that the $CaCO_3$ microstructure on the mesh was severely damaged and detached from the SSM surface (Fig. S15) due to repeated sand impact. However, the mesh pores were partially blocked by the detached tiny $CaCO_3$ and sand particles, resulting in a decrease in water flux. Although the mesh lost its underwater superoleophobicity due to surface structure damage, many $CaCO_3$ particles remained attached around the mesh pores. Hence, it still retained excellent oil-water separation performance, with an oil rejection rate exceeding 99.5%.

In addition, the thermal stability of the mesh was evaluated at 100 ℃, 200 ℃, and 300 ℃, respectively. Fig. 9a-c showed that the surface cubic $CaCO_3$ particles of the $MICP_{(A5)}$-coated SSM remained intact even at temperatures up to 300 ℃. The wettability, water fluxes and oil rejection rates of the $MICP_{(A5)}$-coated SSM at different calcination temperature were measured, as illustrated in Fig. 9d and e. All meshes exhibited superhydrophilicity and underwater superoleophobicity with WCAs of 0° and UWOCAs greater than 150°. Furthermore, all the mesh demonstrated high water flux (> 26464 L m^{-2} h^{-1}) and ultrahigh oil rejection rate (> 99.9%), underscoring its remarkable thermal stability.

4. Conclusions

In summary, the influences of environmental factors, including MS concentration, BS concentration, and temperature, on the wettability and oil-water separation performance of the MICP-coated SSM were thoroughly investigated. With an elevation in temperature or MS concentration, the surface roughness of the $CaCO_3$ coating also experienced a noticeable increase, leading to an enhanced hydrophilicity and oil

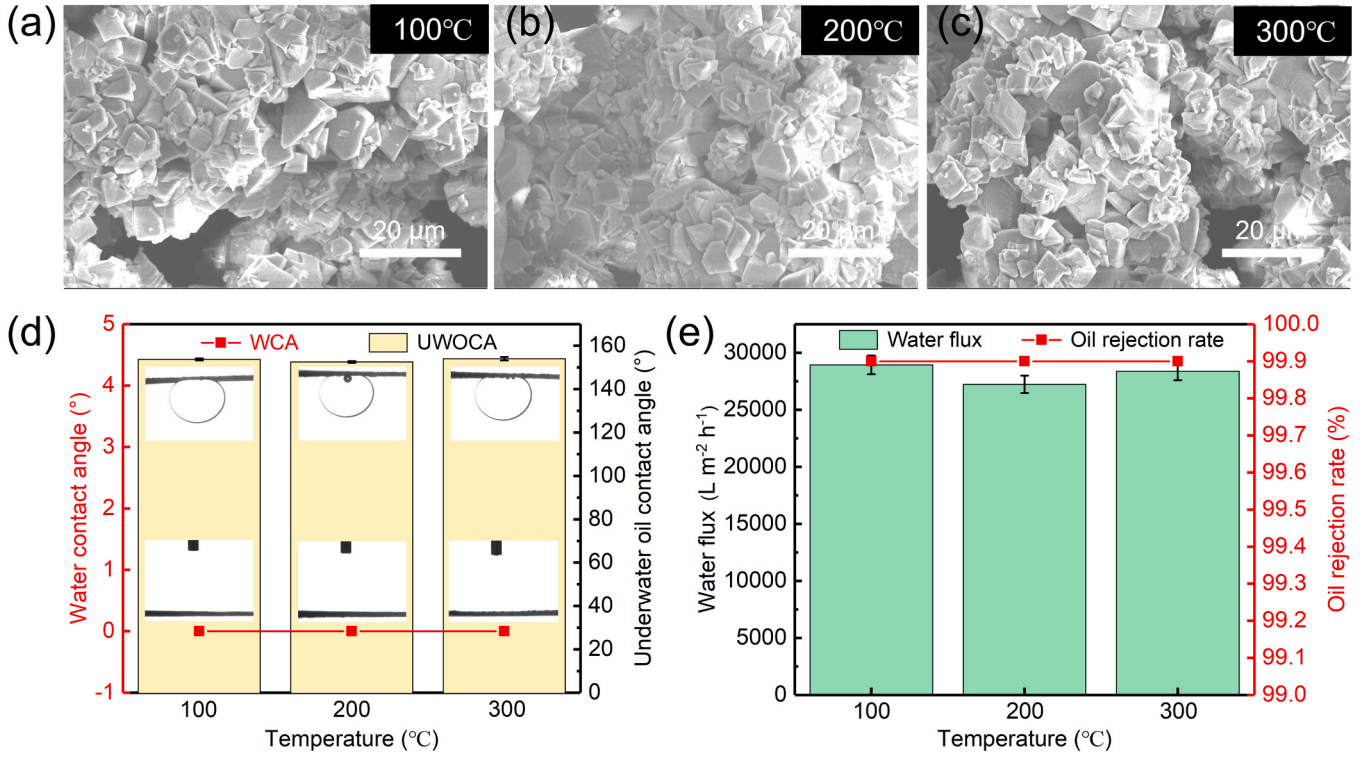

Fig. 9. Thermal stability of the $MICP_{(A5)}$-coated SSM: SEM images of the $MICP_{(A5)}$-coated SSM after calcination at (a) 100 ℃, (b) 200 ℃, and (c) 300 ℃ for 2 h, respectively. The corresponding (d) WCAs, UWOCAs, as well as (e) water fluxes and oil rejection rates.

intrusion pressure of the mesh. In contrast, with an increase in BS concentration, MS concentration, and temperature, the pore size of the mesh decreased, resulting in a significant reduction in water flux. The optimal MICP-coated SSM for oil-water separation was prepared after the MICP process for 24 h at an MS concentration of 0.15 M, BS concentration of 0.1×10^8 cells/mL, and 25 ℃. The obtained MICP-coated SSM with an ultra-high oil intrusion pressure exceeding 3.0 kPa can separate oil-water mixtures with ultrahigh flux (10,942 - 28,644 L m^{-2} h^{-1}), high oil rejection rate (> 99.9%), outstanding reusability (40 cycles) and excellent anti-oil-fouling ability. In addition, the mesh also exhibited ideal chemical stability, thermal stability, and mechanical durability.

CRediT authorship contribution statement

Sikai Tang: Methodology, Investigation, Data curation, Formal analysis, Writing. **Yuze Wang:** Project administration, Supervision, Funding acquisition, Writing – review & editing.

Declaration of Competing Interest

The authors declare that they have no known competing financial interests or personal relationships that could have appeared to influence the work reported in this paper.

Data Availability

Data will be made available on request.

Acknowledgements

This work is financially supported by the Science and Technology Innovation Committee of Shenzhen (Grant No. JCYJ20210324103812033) and the National Natural Science Foundation of China (Grant No. 52171262).

Appendix A. Supporting information

Supplementary data associated with this article can be found in the online version at doi:10.1016/j.jece.2023.111805.

References

[1] C.H. Peterson, S.D. Rice, J.W. Short, D. Esler, J.L. Bodkin, B.E. Ballachey, D. B. Irons, Long-term ecosystem response to the Exxon Valdez oil spill, Science 302 (2003) 2082–2086, https://doi.org/10.101126/science.1084282.
[2] W. Zheng, J. Huang, S. Li, M. Ge, L. Teng, Z. Chen, Y. Lai, Advanced materials with special wettability toward intelligent oily wastewater remediation, ACS Appl. Mater. Interfaces 13 (2021) 67–87, https://doi.org/10.1021/acsami.0c18794.
[3] A. Jernelov, The threats from oil spills: now, then, and in the future, AMBIO 39 (2010) 353–366, https://doi.org/10.1007/s13280-010-0085-5.
[4] M. Peng, Y. Zhu, H. Li, K. He, G. Zeng, A. Chen, Z. Huang, T. Huang, L. Yuan, G. Chen, Synthesis and application of modified commercial sponges for oil-water separation, Chem. Eng. J. 373 (2019) 213–226, https://doi.org/10.1016/j.cej.2019.05.013.
[5] C. Nam, H. Li, G. Zhang, L.R. Lutz, B. Nazari, R.H. Colby, T.C.M. Chung, Practical oil spill recovery by a combination of polyolefin absorbent and mechanical skimmer, ACS Sustain. Chem. Eng. 6 (2018) 12036–12045, https://doi.org/10.1021/acssuschemeng.8b02322.
[6] S.A. Nunes, H.L.F. Magalhaes, S.R. de Farias Neto, A.G.B. Lima, L.P.C. Nascimento, F.P.M. Farias, E.S. Lima, Impact of permeable membrane on the hydrocyclone separation performance for oily water treatment, Membranes 10 (2020) 350, https://doi.org/10.3390/membranes10110350.
[7] B. Huang, X. Li, W. Zhang, C. Fu, Y. Wang, S. Fu, Study on Demulsification-flocculation mechanism of oil-water emulsion in produced water from alkali/surfactant/polymer flooding, Polym. (Basel) 11 (2019) 395, https://doi.org/10.3390/polym11030395.
[8] X. Yin, Z. Wang, Y. Shen, P. Mu, G. Zhu, J. Li, Facile fabrication of superhydrophobic copper hydroxide coated mesh for effective separation of water-in-oil emulsions, Sep. Purif. Technol. 230 (2020) 115856, https://doi.org/10.1016/j.seppur.2019.115856.
[9] Z. Li, T.C. Zhang, T. Mokoba, S. Yuan, Superwetting $Bi_2MoO_6/Cu_3(PO_4)_2$ nanosheet-coated copper mesh with superior anti-oil-fouling and photo-fenton-like catalytic properties for effective oil-in-water emulsion separation, ACS Appl. Mater. Interfaces 13 (2021) 23662–23674, https://doi.org/10.1021/acsami.1c02814.
[10] H. Li, J. Zhang, S. Gan, X. Liu, L. Zhu, F. Xia, X. Luo, Q. Xue, Bioinspired dynamic antifouling of oil-water separation membrane by bubble-mediated shape morphing, Adv. Funct. Mater. 33 (2023) 2212582, https://doi.org/10.1002/adfm.202212582.
[11] X.Q. Zhao, F. Wahid, J.X. Cui, Y.Y. Wang, C. Zhong, Cellulose-based special wetting materials for oil/water separation: a review, Int. J. Biol. Macromol. 185 (2021) 890–906, https://doi.org/10.1016/j.ijbiomac.2021.06.167.
[12] S. Li, J. Huang, Z. Chen, G. Chen, Y. Lai, A review on special wettability textiles: theoretical models, fabrication technologies and multifunctional applications, J. Mater. Chem. A 5 (2017) 31–55, https://doi.org/10.1039/c6ta07984a.
[13] Z. Zhang, H. Dong, Y. Liao, Facile fabrication of SWCNT film-based superhydrophobic cotton fabrics for oil/water separation and self-cleaning, J. Environ. Chem. Eng. 11 (2023) 109570, https://doi.org/10.1016/j.jece.2023.109570.
[14] S. Gan, H. Li, X. Zhu, X. Liu, K. Wei, L. Zhu, B. Wei, X. Luo, J. Zhang, Q. Xue, Constructing scalable membrane with tunable wettability by electrolysis-induced interface pH for oil–water separation, Adv. Funct. Mater. (2023) 2305975, https://doi.org/10.1002/adfm.202305975.
[15] S. Rasouli, N. Rezaei, H. Hamedi, S. Zendehboudi, X. Duan, Superhydrophobic and superoleophilic membranes for oil-water separation application: a comprehensive review, Mater. Des. 204 (2021) 109599, https://doi.org/10.1016/j.matdes.2021.109599.
[16] H. Guan, Z. Cheng, X. Wang, Highly compressible wood sponges with a spring-like lamellar structure as effective and reusable oil absorbents, ACS Nano 12 (2018) 10365–10373, https://doi.org/10.1021/acsnano.8b05763.
[17] J. Wu, Z. Cui, Y. Yu, H. Han, D. Tian, J. Hu, J. Qu, Y. Cai, J. Luo, J. Li, A 3D smart wood membrane with high flux and efficiency for separation of stabilized oil/water emulsions, J. Hazard. Mater. 441 (2023) 129900, https://doi.org/10.1016/j.jhazmat.2022.129900.
[18] E.S. Dmitrieva, T.S. Anokhina, E.G. Novitsky, V.V. Volkov, I.L. Borisov, A. V. Volkov, Polymeric membranes for oil-water separation: a review, Polymers 14 (2022) 980, https://doi.org/10.3390/polym14050980.
[19] N. Zhang, X. Yang, Y. Wang, Y. Qi, Y. Zhang, J. Luo, P. Cui, W. Jiang, A review on oil/water emulsion separation membrane material, J. Environ. Chem. Eng. 10 (2022) 107257, https://doi.org/10.1016/j.jece.2022.107257.
[20] M. Zhu, Y. Liu, M. Chen, Z. Xu, L. Li, Y. Zhou, Metal mesh-based special wettability materials for oil-water separation: a review of the recent development, J. Petrol. Sci. Eng. 205 (2021) 108889, https://doi.org/10.1016/j.petrol.2021.108889.
[21] C. Fu, L. Gu, Z. Zeng, Q. Xue, One-Step Transformation of metal meshes to robust superhydrophobic and superoleophilic meshes for highly efficient oil spill cleanup and oil/water separation, ACS Appl. Mater. Interfaces 12 (2020) 1850–1857, https://doi.org/10.1021/acsami.9b17052.
[22] J. Wang, S. Liu, Fabrication of water-repellent double-layered polydopamine/copper films on mesh with improved abrasion and corrosion resistance by solution-phase reduction for oily wastewater treatment, Sep. Purif. Technol. 233 (2020) 116005, https://doi.org/10.1016/j.seppur.2019.116005.
[23] Z. Xue, Y. Cao, N. Liu, L. Feng, L. Jiang, Special wettable materials for oil/water separation, J. Mater. Chem. A 2 (2014) 2445–2460, https://doi.org/10.1039/c3ta13397d.
[24] M. Liu, S. Wang, Z. Wei, Y. Song, L. Jiang, Bioinspired design of a superoleophobic and low adhesive water/solid interface, Adv. Mater. 21 (2009) 665–669, https://doi.org/10.1002/adma.200801782.
[25] Z. Xue, S. Wang, L. Lin, L. Chen, M. Liu, L. Feng, L. Jiang, A novel superhydrophilic and underwater superoleophobic hydrogel-coated mesh for oil/water separation, Adv. Mater. 23 (2011) 4270–4273, https://doi.org/10.1002/adma.201102616.
[26] C. Wu, Y. Zhang, Q. Zhao, Y. Li, B. Zhang, Ultrahigh throughput and efficient separation of oil/water mixtures using superhydrophilic multi-scale CuBTC-coated meshes, Sep. Purif. Technol. 279 (2021) 119802, https://doi.org/10.1016/j.seppur.2021.119802.
[27] S. Zarghami, T. Mohammadi, M. Sadrzadeh, B. Van der Bruggen, Superhydrophilic and underwater superoleophobic membranes - a review of synthesis methods, Prog. Polym. Sci. 98 (2019) 101166, https://doi.org/10.1016/j.progpolymsci.2019.101166.
[28] L. Qiu, Y. Sun, Z. Guo, Designing novel superwetting surfaces for high-efficiency oil–water separation: design principles, opportunities, trends and challenges, J. Mater. Chem. A 8 (2020) 16831–16853, https://doi.org/10.1039/d0ta02997a.
[29] C. Chen, L. Chen, S. Chen, Y. Yu, D. Weng, A. Mahmood, G. Wang, J. Wang, Preparation of underwater superoleophobic membranes via TiO_2 electrostatic self-assembly for separation of stratified oil/water mixtures and emulsions, J. Membr. Sci. 602 (2020) 117976, https://doi.org/10.1016/j.memsci.2020.117976.
[30] J. Pan, Y. Ge, Low-cost and high-stability superhydrophilic/underwater superoleophobic NaA zeolite/copper mesh composite membranes for oil/water separation, Surf. Interfaces 37 (2023) 102703, https://doi.org/10.1016/j.surfin.2023.102703.
[31] Y. Xie, Y.H. Gu, J. Meng, X. Yan, Y. Chen, X.J. Guo, W.Z. Lang, Ultrafast separation of oil/water mixtures with layered double hydroxide coated stainless steel meshes (LDH-SSMs), J. Hazard. Mater. 398 (2020) 122862, https://doi.org/10.1016/j.jhazmat.2020.122862.
[32] P. Raturi, K. Yadav, J.P. Singh, ZnO-nanowires-coated smart surface mesh with reversible wettability for efficient on-demand oil/water separation, ACS Appl. Mater. Interfaces 9 (2017) 6007–6013, https://doi.org/10.1021/acsami.6b14448.

[33] P. Song, Q. Lu, Porous clusters of metal-organic framework coated stainless steel mesh for highly efficient oil/water separation, Sep. Purif. Technol. 238 (2020) 116454, https://doi.org/10.1016/j.seppur.2019.116454.
[34] K. Li, W. Chen, W. Wu, Z. Pan, Z. Liang, J. Gan, Facile fabrication of superhydrophilic/underwater superoleophobic polyvinyl acetate/sodium silicate composite coating for the effective water/oil separation and the study on the anti-fouling property, durability and separation mechanism, Prog. Org. Coat. 150 (2021) 105979, https://doi.org/10.1016/j.porgcoat.2020.105979.
[35] X. Liu, J. Zhou, Z. Xue, J. Gao, J. Meng, S. Wang, L. Jiang, Clam's shell inspired high-energy inorganic coatings with underwater low adhesive superoleophobicity, Adv. Mater. 24 (2012) 3401–3405, https://doi.org/10.1002/adma.201200797.
[36] W. Chen, P. Zhang, R. Zang, J. Fan, S. Wang, B. Wang, J. Meng, Nacre-inspired mineralized films with high transparency and mechanically robust underwater superoleophobicity, Adv. Mater. 32 (2020) e1907413, https://doi.org/10.1002/adma.201907413.
[37] L. Li, Y. Yang, Y. Lv, P. Yin, T. Lei, Porous calcite $CaCO_3$ microspheres: preparation, characterization and release behavior as doxorubicin carrier, Colloids Surf. B 186 (2020) 110720, https://doi.org/10.1016/j.colsurfb.2019.110720.
[38] J. Dai, L. Wang, Y. Wang, S. Tian, X. Tian, A. Xie, R. Zhang, Y. Yan, J. Pan, Robust nacrelike graphene oxide-calcium carbonate hybrid mesh with underwater superoleophobic property for highly efficient oil/water separation, ACS Appl. Mater. Interfaces 12 (2020) 4482–4493, https://doi.org/10.1021/acsami.9b18664.
[39] S. Yu, W. Chen, Y. Wang, R. Zhao, R. Zang, J. Gu, J. Meng, S. Wang, Nacre-inspired biomineralized mesh toward scalable and robust oil–water separation with high efficiency, Adv. Mater. Interfaces 8 (2021) 2100852, https://doi.org/10.1002/admi.202100852.
[40] M. Li, Y. Chen, L.B. Mao, Y. Jiang, M.F. Liu, Q. Huang, Z. Yu, S. Wang, S.H. Yu, C. Lin, X.Y. Liu, H. Colfen, Seeded mineralization leads to hierarchical $CaCO_3$ thin coatings on fibers for oil/water separation applications, Langmuir 34 (2018) 2942–2951, https://doi.org/10.1021/acs.langmuir.7b03813.
[41] E. Ortega-Villamagua, M. Gudino-Gomezjurado, A. Palma-Cando, Microbiologically induced carbonate precipitation in the restoration and conservation of cultural heritage materials, Molecules 25 (2020) 5499, https://doi.org/10.3390/molecules25235499.
[42] Y. Xiao, Y. Wang, S. Wang, T.M. Evans, A.W. Stuedlein, J. Chu, C. Zhao, H. Wu, H. Liu, Homogeneity and mechanical behaviors of sands improved by a temperature-controlled one-phase MICP method, Acta Geotech. 16 (2021) 1417–1427, https://doi.org/10.1007/s11440-020-01122-4.
[43] Y. Wang, C. Konstantinou, K. Soga, G. Biscontin, A.J. Kabla, Use of microfluidic experiments to optimize MICP treatment protocols for effective strength enhancement of MICP-treated sandy soils, Acta Geotech. 17 (2022) 3817–3838, https://doi.org/10.1007/s11440-022-01478-9.
[44] D. Zhang, M.A. Shahin, Y. Yang, H. Liu, L. Cheng, Effect of microbially induced calcite precipitation treatment on the bonding properties of steel fiber in ultra-high performance concrete, J. Build. Eng. 50 (2022) 104132, https://doi.org/10.1016/j.jobe.2022.104132.
[45] T. Liu, Z. Guo, Z. Zeng, N. Guo, Y. Lei, T. Liu, S. Sun, X. Chang, Y. Yin, X. Wang, Marine bacteria provide lasting anticorrosion activity for steel via biofilm-induced mineralization, ACS Appl. Mater. Interfaces 10 (2018) 40317–40327, https://doi.org/10.1021/acsami.8b14991.
[46] Z. He, Y. Xu, W. Wang, X. Yang, Z. Jin, D. Zhang, X. Pan, Synergistic mechanism and application of microbially induced carbonate precipitation (MICP) and inorganic additives for passivation of heavy metals in copper-nickel tailings, Chemosphere 311 (2023) 136981, https://doi.org/10.1016/j.chemosphere.2022.136981.
[47] S. Tang, X. Chang, M. Li, T. Ge, S. Niu, D. Wang, Y. Jiang, S. Sun, Fabrication of calcium carbonate coated-stainless steel mesh for efficient oil-water separation via bacterially induced biomineralization technique, Chem. Eng. J. 405 (2021) 126597, https://doi.org/10.1016/j.cej.2020.126597.
[48] S. Tang, S. Sun, T. Liu, M. Li, Y. Jiang, D. Wang, N. Guo, Z. Guo, X. Chang, Bionic engineering-induced formation of hierarchical structured minerals with superwetting surfaces for oil-water separation, J. Membr. Sci. 669 (2023) 121261, https://doi.org/10.1016/j.memsci.2022.121261.
[49] S. Stocks-Fischer, J.K. Galinat, S.S. Bang, Microbiological precipitation of $CaCO_3$, Soil Biol. Biochem. 31 (1999) 1563–1571, https://doi.org/10.1016/S0038-0717(99)00082-6.
[50] J.T. DeJong, M.B. Fritzges, K. Nüsslein, Microbially induced cementation to control sand response to undrained shear, J. Geotech. Geoenviron. Eng. 132 (2006) 1381–1392, https://doi.org/10.1061/(ASCE)1090-0241(2006)132:11(1381).
[51] C. Lv, C.-S. Tang, C. Zhu, W.-Q. Li, T.-Y. Chen, L. Zhao, X.-H. Pan, Environmental dependence of microbially induced calcium carbonate crystal precipitations: experimental evidence and insights, J. Geotech. Geoenviron. Eng. 148 (2022), https://doi.org/10.1061/(asce)gt.1943-5606.0002827.
[52] Y. Wang, Y. Wang, K. Soga, J.T. DeJong, A.J. Kabla, Microscale investigations of temperature-dependent microbially induced carbonate precipitation (MICP) in the temperature range 4–50 °C, Acta Geotech. 18 (2023) 2239–2261, https://doi.org/10.1007/s11440-022-01664-9.
[53] X. Gao, L.P. Xu, Z. Xue, L. Feng, J. Peng, Y. Wen, S. Wang, X. Zhang, Dual-scaled porous nitrocellulose membranes with underwater superoleophobicity for highly efficient oil/water separation, Adv. Mater. 26 (2014) 1771–1775, https://doi.org/10.1002/adma.201304487.
[54] B.-S. Kim, P. Harriott, Critical entry pressure for liquids in hydrophobic membranes, J. Colloid Interf. Sci. 115 (1986) 1–8, https://doi.org/10.1016/0021-9797(87)90002-6.
[55] Y. Sun, Y. Liu, B. Xu, J. Chen, W. Yuan, C. Jiang, D. Wang, H. Wang, Simultaneously achieving high-effective oil-water separation and filter media regeneration by facile and highly hydrophobic sand coating, Sci. Total Environ. 800 (2021) 149488, https://doi.org/10.1016/j.scitotenv.2021.149488.
[56] M. Paul, D. Upadhaya, D. Dhar Purkayastha, M.G. Krishna, $ZnO/WO_3{\cdot}H_2O$ micro-nanostructures coated mesh for efficient separation of oil-water mixture, Appl. Surf. Sci. 583 (2022) 152476, https://doi.org/10.1016/j.apsusc.2022.152476.
[57] G. Qi, K. Guo, J. Yang, Y. Wang, Z. Wang, Z. Yuan, A stable underwater superoleophobic membrane constructed by CuO oriented rods and PAA water-adsorbent resin for fast and high efficient oil–water separation, Sep. Purif. Technol. 294 (2022) 121175, https://doi.org/10.1016/j.seppur.2022.121175.
[58] Y. Zhang, H. Wang, B. Liu, X. Zhao, Y. Wei, $NiCo_2O_4$ hierarchical structure coated mesh with long-term stable underwater superoleophobicity for high-efficient, high-flux oil-water separation, Appl. Surf. Sci. 504 (2020) 144598, https://doi.org/10.1016/j.apsusc.2019.144598.
[59] Y. Liu, L. Wang, H. Lu, Z. Huang, Achieving effective oil/water separation with bicomponent supramolecular hydrogel paint coated metal mesh, ACS Appl. Polym. Mater. 2 (2020) 4770–4778, https://doi.org/10.1021/acsapm.0c00764.
[60] C. Huang, M. Zhu, Y. Mao, Solventless polymer-grafted mesh for rapid and efficient oil–water separation, ACS Appl. Polym. Mater. 5 (2023) 3801–3808, https://doi.org/10.1021/acsapm.3c00399.
[61] J. Myeong, P.R. Deshmukh, W. Gyu Shin, Facile preparation of superhydrophilic and underwater superoleophobic stainless steel mesh for oil–water separation, J. Ind. Eng. Chem. 120 (2023) 398–409, https://doi.org/10.1016/j.jiec.2022.12.047.
[62] L. Xia, F. Chen, J. Chao, D. Zhang, Y. Tian, D. Zhang, Femtosecond laser engineered eggshell membrane for durable oil/water separation under harsh conditions, J. Membr. Sci. 668 (2023) 121242, https://doi.org/10.1016/j.memsci.2022.121242.
[63] Y. Yin, L. Zhu, X. Chang, J. Xue, S. Yu, X. Li, Q. Xue, Bioinspired anti-oil-fouling hierarchical structured membranes decorated with urchin-like alpha-FeOOH particles for efficient oil/water mixture and crude oil-in-water emulsion separation, ACS Appl. Mater. Interfaces 12 (2020) 50962–50970, https://doi.org/10.1021/acsami.0c11677.
[64] A. Shome, A. Das, N. Rawat, A.M. Rather, U. Manna, Reduction of imine-based cross-linkages to achieve sustainable underwater superoleophobicity that performs under challenging conditions, J. Mater. Chem. A 8 (2020) 15148–15156, https://doi.org/10.1039/d0ta04426a.
[65] H. Li, Y. Yin, L. Zhu, Y. Xiong, X. Li, T. Guo, W. Xing, Q. Xue, A hierarchical structured steel mesh decorated with metal organic framework/graphene oxide for high-efficient oil/water separation, J. Hazard. Mater. 373 (2019) 725–732, https://doi.org/10.1016/j.jhazmat.2019.04.009.